Earth and Planetary Science Letters 296 (2010) 181–194

Contents lists available at ScienceDirect

Earth and Planetary Science Letters

journal homepage: www.elsevier.com/locate/epsl

The vertical separation of mainshock rupture and microseismicity at Qeshm island in the Zagros fold-and-thrust belt, Iran

E. Nissen [a,*], F. Yamini-Fard [b], M. Tatar [b], A. Gholamzadeh [b,1], E. Bergman [c], J.R. Elliott [d], J.A. Jackson [a], B. Parsons [d]

[a] COMET, Bullard Laboratories, Department of Earth Sciences, University of Cambridge, Madingley Road, Cambridge CB3 0EZ, UK
[b] International Institute of Earthquake Engineering and Seismology, PO Box 19395-3913, Tehran, Iran
[c] Department of Physics, University of Colorado, Boulder, CO 80309-0390, USA
[d] COMET, Department of Earth Sciences, University of Oxford, Parks Road, Oxford OX1 3PR, UK

ARTICLE INFO

Article history:
Received 11 January 2010
Received in revised form 24 March 2010
Accepted 24 April 2010
Available online 9 June 2010

Editor: T.M. Harrison

Keywords:
Zagros
InSAR
earthquakes
source parameters
folding

ABSTRACT

We investigate the depth and geometry of faulting within a cluster of buried, reverse faulting earthquakes that struck Qeshm island, in the Zagros fold-and-thrust belt, over a four year period between November 2005 and July 2009. Of particular interest is our observation that there was a vertical separation between the largest two earthquakes (M_w 5.8 and 5.9), which ruptured the lower parts of a ~10-km thick sedimentary cover, and microseismicity recorded by a local network after the first, M_w 5.8 event, which was concentrated within the underlying basement at depths of 10–20 km. Although measured in different ways — the largest three earthquakes using radar interferometry, moderate-sized events with teleseismically-recorded, long-period waveforms, and the microseismicity using data from a local seismic network — we used consistent velocity and elastic parameters in all our modelling, and the observed vertical separation is robust and resolvable. We suggest that it reflects the influence of the Proterozoic Hormuz salt, a weak layer at the base of the sedimentary cover across which rupture failed to propagate. Because the full thickness of the seismogenic layer failed to rupture during the largest earthquakes in the sequence, the lower, unruptured part may constitute a continued seismic hazard to the region. Considering the rarity of earthquakes larger than M_w 6.2 in the Zagros Simply Folded Belt, we suggest that the Hormuz salt forms an important, regional barrier to rupture, not just a local one. Finally, we note that buried faulting involved in the largest earthquakes is almost perpendicular to the trend of an anticline exposed at the surface immediately above them. This suggests that locally, faulting and folding are decoupled, probably along a weak layer of marls or evaporites in the middle part of the sedimentary cover.

1. Introduction

The Zagros mountains in south-western Iran are one of the most rapidly-deforming and seismically-active fold-and-thrust belts in the world, accommodating almost half of the present-day shortening between Arabia and Eurasia (Fig. 1). Because direct observations of earthquake faulting are possible here, and can be made relatively frequently, the Zagros potentially provides a superb present-day analogue for fold-and-thrust belts elsewhere on the continents, including those which are no longer active. However, earthquakes in the Zagros only very rarely rupture the surface and so far, most observations of faulting in moderate-sized earthquakes have been inferred from seismology (e.g. Adams et al., 2009; Talebian and Jackson, 2004). Errors in the best teleseismically-recorded epicenters and waveform-constrained depths — 10–15 km and ~4 km, respectively (Engdahl et al., 2006) — are such that the precise location and geometry of earthquake faulting, and thus its relationship to the geological structure, have proven difficult to ascertain.

One important issue which remains unresolved, and which is the focus of this study, concerns the relative behaviour and seismogenic potential of the crystalline basement and the overlying sedimentary cover. The cover is up to 10–15-km thick and encompasses a mixture of strong units (mainly platform carbonates) and weaker evaporites, marls and shales. Although the occurrence of small and moderate magnitude earthquakes (M_w 4.5–5.5) at these shallow depths is well resolved (Adams et al., 2009; Lohman and Simons, 2005; Roustaei et al., 2010; Talebian and Jackson, 2004), it is not clear whether the cover is strong enough to generate larger events (M_w ~6), or whether these are restricted to the basement. There has also been much debate about the

* Corresponding author.
E-mail address: ekn20@cam.ac.uk (E. Nissen).
[1] Present address: University of Hormozgan, Bandar Abbas, Iran.

0012-821X/$ – see front matter.
doi:10.1016/j.epsl.2010.04.049

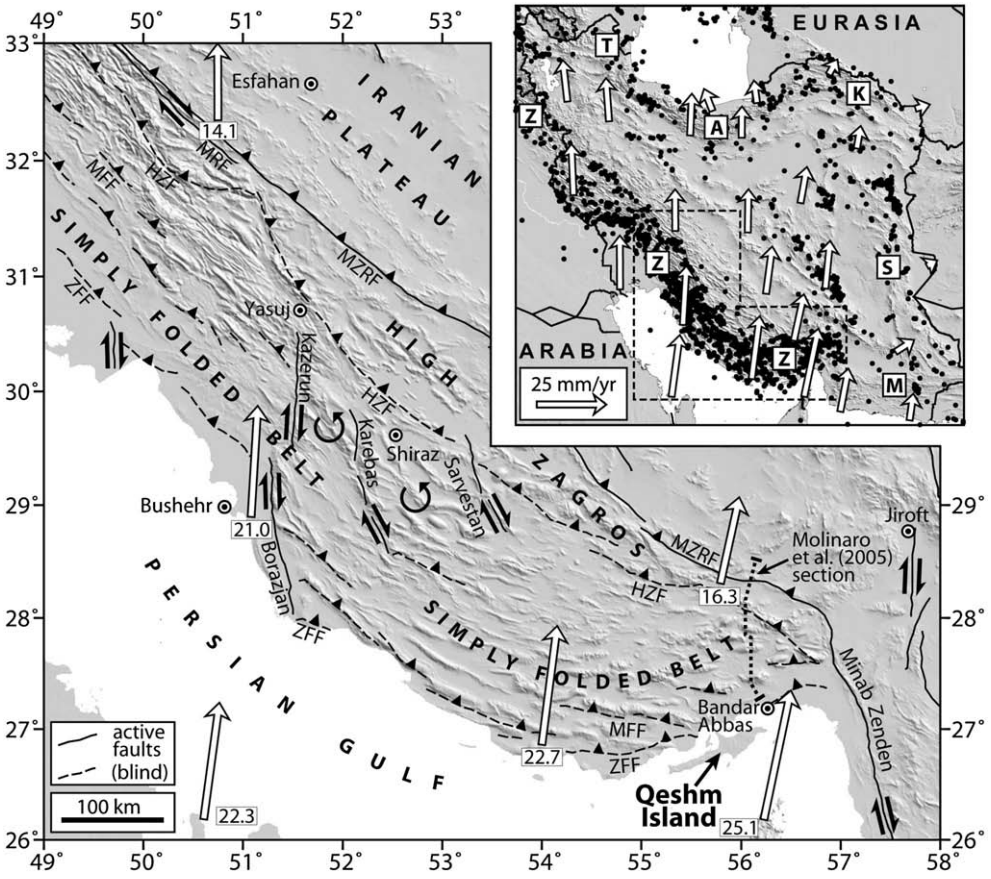

Fig. 1. Inset: topographic map of Iran, illuminated from the NE. Black dots are earthquakes from an updated version of the Engdahl et al. (1998) catalogue, and arrows are GPS velocities relative to stable Eurasia from Vernant et al. (2004). Major earthquake belts are marked Z (Zagros), T (Talesh), A (Alborz), K (Kopeh Dag), S (Sistan) and M (Makran). The location of the main figure is outlined by a dashed black line. Main figure: the south-eastern Zagros, with GPS velocities (as above, with rates in mm year^{-1}) and major faults (black lines, dashed if blind). The suture between rocks of the Arabian margin and those of central Iran follows the MZRF (Main Zagros Reverse Fault) and the right-lateral MRF (Main Recent Fault), and the "master blind thrusts" of Berberian (1995) are marked HZF (High Zagros Fault), MFF (Mountain Front Fault) and ZFF (Zagros Foredeep Fault). The dotted line north of Bandar Abbas marks the cross-section of Molinaro et al. (2005), from which the stratigraphic thicknesses in Fig. 2 were compiled.

extent to which the weaker units, especially the Proterozoic Hormuz salt at the base of the cover, separate deformation in underlying and overlying layers.

A recent cluster of eleven, M_w 5–6 earthquakes at Qeshm island (SE Zagros) provide an opportunity to investigate these problems. In this paper we establish the vertical distribution of faulting that occurred during these earthquakes, using detailed observations from radar interferometry (InSAR), locally-recorded seismic data, and teleseismically-recorded body-waves. By combining these different methodologies we are able to locate the causative faulting more precisely than would be possible using any single method on its own.

2. Geological and tectonic setting

2.1. Overview

The Zagros mountains extend ~1800 km from northern Iraq to the Strait of Hormuz (inset, Fig. 1), and comprise the deformed, north-eastern margin of the Arabian plate following its collision with central Iran in the Miocene, Oligocene or Eocene (Agard et al., 2005; Allen and Armstrong, 2008; McQuarrie et al., 2003). Present-day shortening across the range, measured with GPS, increases from ~4 mm year^{-1} in the NW to ~9 mm year^{-1} in the SE (Vernant et al., 2004; Walpersdorf et al., 2006).

The Zagros can be divided into two distinct zones, based on topography, geomorphology, exposed stratigraphy, and seismicity. The north-eastern zone, bordering the Iranian plateau, is known as the High Zagros (Fig. 1). This area contains Paleozoic and Mesozoic sediments and ophiolites, cut by major thrust and reverse faults which are well-exposed at the surface (Berberian, 1995). However, present-day seismicity in the High Zagros is relatively low, except for the active Main Recent Fault, which accommodates the right-lateral component of Arabia–Iran motion in the NW (e.g. Peyret et al., 2008; Talebian and Jackson, 2002).

The south-western zone, bordering the Persian Gulf, is known as the Simply Folded Belt (SFB) (Fig. 1). This area contains a thick sedimentary cover spanning the entire Phanerozoic, which is folded into parallel trains of 'whaleback' anticlines and synclines (e.g. Colman-Sadd, 1978; Falcon, 1969; O'Brien, 1957; Stöcklin, 1968). It is also the most seismically-active part of the range, with frequent earthquakes of M_w 5–6 and occasional larger events up to M_w 6.7. Observations from stratigraphy, GPS and geomorphology suggest that deformation migrated from the High Zagros to the SFB at an earlier stage in the collision (Hessami et al., 2001b; Oveisi et al., 2009; Walpersdorf et al., 2006).

2.2. Stratigraphy

The sedimentary cover in the Simply Folded Belt plays an important role in its deformation and warrants further description. Fig. 2 shows a simplified stratigraphy for the SE Zagros, close to where our study is based, from Molinaro et al. (2005). At the base of the sequence is the Proterozoic Hormuz Salt formation, which comes to the surface in salt plugs and diapirs across the central and south-eastern SFB (e.g. Kent, 1979). Paleozoic and lower Mesozoic strata comprise conglomerates and massive limestones and dolomites, collectively termed the 'Competent Group.' Upper Cretaceous to middle Miocene rocks

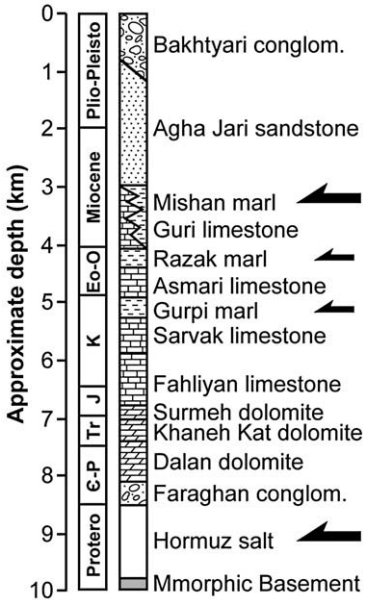

Fig. 2. Simplified stratigraphic column for the far south-eastern Zagros, from work by Molinaro et al. (2005) on the mainland north of Qeshm island (dotted line, Fig. 1). The depths are poorly constrained and should only be considered approximate. Possible detachment levels are picked out by black arrows. The Razak marls are the lateral equivalent of the better-known Gachsaran evaporite formation (found in the central Simply Folded Belt). The 'Competent Group' comprises the package of relatively competent sediments from the Cambrian Faraghan conglomerate up to the Cretaceous Sarvak limestone.

encompass a more mixed sequence of mechanically-weak marls and evaporites (e.g. Gurpi, Razak and Mishan formations) interspersed with competent limestones (e.g. Asmari and Guri formations). Miocene to Recent strata comprise coarse, clastic sediments, and signify the onset of regional continental shortening and uplift.

The full stratigraphic thickness is estimated at ~12 km in the central SFB (Colman-Sadd, 1978) and ~10 km in the far south-east, close to our study area (Molinaro et al., 2005). In the absence of published seismic reflection or refraction data, it is not clear whether these values also reflect depths to basement, or whether the sediments have been substantially thickened by faulting and folding. Analysis of aeromagnetic data for the mainland Zagros (Kugler, 1973; Morris, 1977) reveals a wide range of basement depths, between 4 km and 18 km (Talebian, 2003). However, these estimates rely on long-wavelength magnetic signals, and in most places the precise local depth to basement is poorly constrained. One exception is the Ghir region in the central SFB (28° N, 53° E), where arrival times of locally-recorded micro-earthquakes were inverted to establish a basement depth of ~11 km (Hatzfeld et al., 2003).

2.3. Seismicity

Fig. 3 shows earthquake focal mechanisms with centroid depths in the central and SE Zagros, from Talebian and Jackson (2004); Adams et al. (2009) and Roustaei et al. (2010). In the SFB, most earthquakes occur on reverse faults that strike parallel with the trend of the range and have steep dips (30°–60°), possibly inherited from older normal faults in the stretched Arabian margin (Jackson, 1980). A number of N–S right-lateral strike-slip faults are also active in the central SFB (Figs. 1, 3); with NW–SE trending *T*-axes, these accommodate some range-parallel extension (Authemayou et al., 2009; Baker et al., 1993; Hessami et al., 2001a; Talebian and Jackson, 2004).

The centroid depths of moderate-to-large magnitude earthquakes lie in the range 4–18 km, indicating that earthquake faulting is generated both in the basement and in the sedimentary cover (Adams et al., 2009; Maggi et al., 2000; Talebian and Jackson, 2004). Earthquake fault dislocation models from radar interferometry provide further confirmation that the sedimentary cover is seismogenic. Lohman and Simons (2005) established depths of 1–5 km for five events of M_w 4.5–5.5, and Roustaei et al. (2010) determined top and bottom depths of ~5 km and ~9 km for the M_w 5.7 and 5.5 Fin earthquakes (25 March 2006; inset, Fig. 3). The only known case of surface rupture in a thrust event is for the 10 November 1990 Furg earthquake, which occurred on the High Zagros Fault at the very northern edge of the SFB (Walker et al., 2005; inset, Fig. 3).

Despite the frequency of earthquakes in the SFB, seismic deformation can only account for a small proportion of the overall convergence across the range, the rest being accommodated aseismically. Summing moment tensors for large ($M_w \geq 6$) earthquakes over the period 1908–1981 and assuming a seismogenic layer thickness of 15 km, Jackson and McKenzie (1988) showed that 4–7% of the shortening rate calculated from relative plate motions is released seismically. Updating the earthquake catalogue through to 2002 and using GPS-derived convergence rates, Masson et al. (2005) calculated that large earthquakes are responsible for less than 3% of the present-day shortening rate across the Zagros. Had it been possible to include smaller earthquakes ($M_w < 6$) in this calculation the seismic contribution would have been higher, but still probably not more than 10–15% of the total convergence rate (Jackson and McKenzie, 1988).

2.4. Folding

In the main part of the SFB, much of the shortening at the surface is accommodated by folding. Fold shapes are expressed in resistant units such as the Asmari limestone, such that anticlines form the high topography of the region and synclines the valleys. Individual folds are typically ~10 km in width and up to 100 km in length. In the main part they are symmetric, although some anticlines verge southwards with steepened or even overturned southern limbs.

Some authors have proposed that surface folding represent buckling of sediments along detachments within or at the base of the sedimentary cover ('detachment folding'), with few faults within the cover itself (e.g. (Stöcklin, 1968; Falcon, 1969; Colman-Sadd, 1978; Jackson, 1980; Hessami et al., 2001b)). An alternative view has folding produced by a mixture of fault propagation and fault-bending above reverse faults nucleating within the basement (Berberian, 1995, e.g.) or the lower part of the sedimentary cover (e.g. Alavi, 2007; McQuarrie, 2004). Many of the asymmetric folds correspond to a significant change in elevation and stratigraphical level at the surface. Berberian (1995) proposed that such structures represent the surface expression of a discrete number of N-dipping basement thrusts, which he called "master blind thrusts" (Fig. 1). These are interpreted to pass upwards into the sedimentary cover, where locally they control folding, but do not necessarily break the surface (e.g. Blanc et al., 2003). A test of this hypothesis would be the existence of bands of basement seismicity along these steps in elevation and stratigraphy, but so far the number of large earthquakes that have occurred unequivocally within the basement is too small for this to be done (Fig. 3).

Finally, some authors have proposed a two-stage model of deformation for the SFB, involving (at different times) both detachment and forced folding (Molinaro et al., 2005; Sherkati et al., 2006). In the first stage, shortening of the basement is accommodated by faulting, and shortening of the cover by buckling. In the second stage, migration of mobile Hormuz salt into the cores of anticlines promotes faulting within the lower sedimentary cover, thereby steepening some of the SW-facing fold limbs. These faults propagate upwards from a detachment in the Hormuz salt, or from deeper faults which break through the basement–cover interface. This two-stage model is derived from an apparent overprinting of detachment folding with forced folding in the far south-eastern SFB, ~50 km east of our own study area (Molinaro et al., 2005).

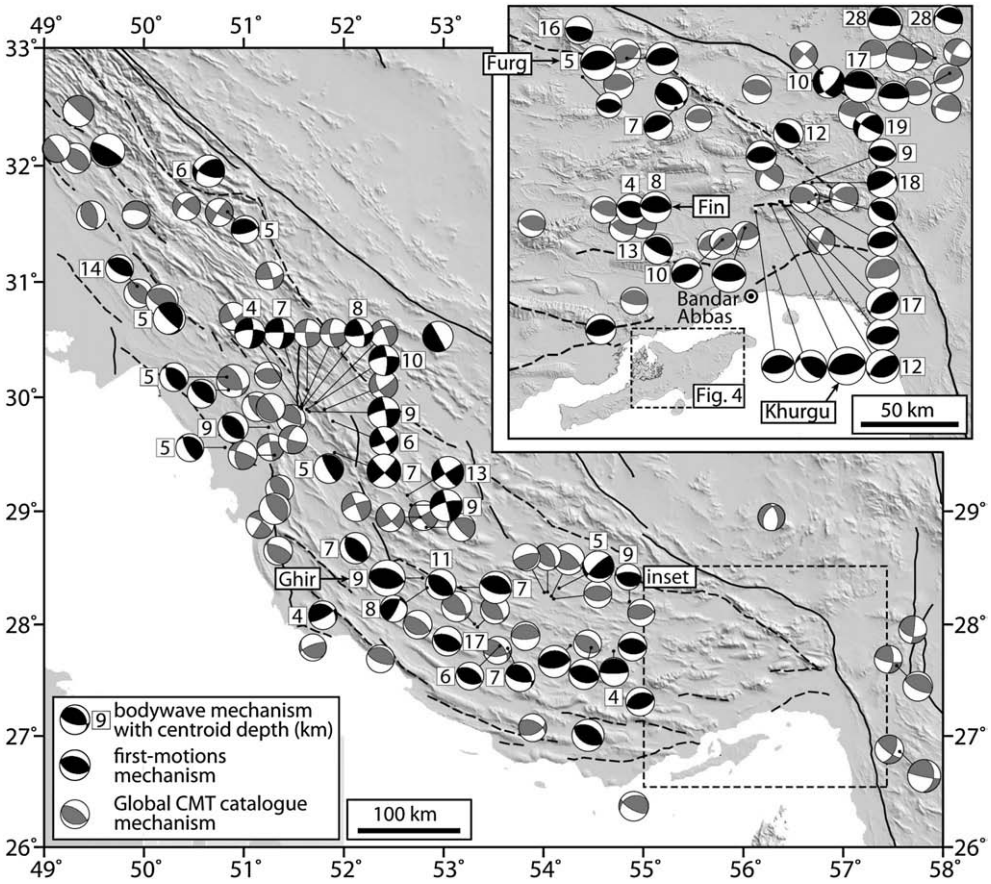

Fig. 3. Earthquake focal mechanisms in the south-eastern Zagros (for simplicity, we do not plot the Qeshm island earthquakes on this figure). Black mechanisms span the period 1964–2009 and are from body-wave modelling (with centroid depths in km) or first-motion polarities (without centroid depths). These are from Talebian and Jackson (2004) and references therein, Adams et al. (2009) and Roustaei et al. (2010). Grey mechanisms are from the Global CMT catalogue and span the period 1976–2009. All earthquakes are plotted at their Engdahl et al. (2006) epicenters. Specific earthquakes discussed in the text are labelled Ghir (10 April 1972), Khurgu (21 March 1977), Furg (10 November 1990) and Fin (25 March 2006).

Unfortunately, different competing models of fold generation can all be consistent with the structure observed at the surface. For instance, balanced cross-sections across a particular part of the SFB show fault propagation and fault-bend folding above faults in the lower crust in McQuarrie (2004); but detachment folding with faulting restricted to the basement in Mouthereau et al. (2007). Furthermore, there are few published seismic reflection data with which to constrain the structure at depth (Jahani et al., 2009; Sherkati et al., 2005).

By establishing the precise depth and geometry of earthquake faulting, observations of surface deformation from InSAR can potentially help discriminate between these models. However, such studies are so far restricted to a few individual earthquakes. Those studied by Lohman and Simons (2005) occurred within the cover but were small events (M_w 4.5–5.5), rupturing faults that would not be expected to control the large-scale deformation. The somewhat larger (M_w 5.5 and 5.7) 25 March 2006 Fin earthquakes probably ruptured the Competent Group in the lower sedimentary cover, but there was no spatial correlation between the causative faulting and overlying folds (Roustaei et al., 2010). The Qeshm island sequence described here includes two larger earthquakes (M_w 6), and thus potentially offers important evidence for relations between buried faulting and surface structure.

3. The Qeshm island earthquake sequence

3.1. Overview of Qeshm island

At 110 km in length, and between 10 km and 35 km in width, Qeshm is the largest of the Persian Gulf islands (Fig. 1). It trends ENE along the northern Strait of Hormuz, separated from mainland Iran by the narrow Clarence Strait (or Strait of Khuran). Its surface geology comprises gentle folds of Lower Miocene Mishan marls, Upper Miocene to Pliocene Agha Jari sandstones and Lahbari marls, and Plio-Pleistocene Kharg limestones (the lateral equivalent of the Bakhtyari conglomerates found in the mainland Zagros). Most folds are oriented ENE–WSW, parallel to the trend of the island itself, the exception being the NW–SE-trending Laft anticline, which forms a distinctive, thumb-shaped peninsula on the island's northern coastline (Fig. 4a). Dome-shaped plugs of Hormuz salt are exposed at Kuh-e-Namakdan, in SW Qeshm island, and at Hengam, a separate island off the southern Qeshm coastline.

Raised marine terraces are observed around much of the Qeshm coastline, indicating late Quaternary tectonic uplift of parts of the island (Haghipour and Fontugne, 1993; Pirazzoli et al., 2004; Reyss et al., 1998). Reef and beach deposits uncomformably overlie folded Neogene sediments on as many as eighteen separate terraces, ranging from the present-day littoral zone up to 220 m above sea level. Corals dated with Th/U and electron spin resonance (ESR) and ascribed to Marine Isotope Stage 5 yield late Quaternary uplift rates of ~0.2 mm year^{-1} (Pirazzoli et al., 2004; Reyss et al., 1998).

There are records of several earthquakes on or near Qeshm island prior to the 2005–2009 sequence, including destructive historical events in 1360, 1703, 1884, 1897, 1902 and 1905 (Berberian and Papastamatiou, 1978), and a number of instrumentally-recorded M_w 5–5.5 earthquakes in the 1960s–1980s. The latest period of activity commenced on 27 November 2005 with a M_w 6 earthquake in central Qeshm island, and was followed by ten more M_w 5–6 earthquakes and numerous smaller shocks in the subsequent four year period (Table 1). In the remainder of this section, we describe and model

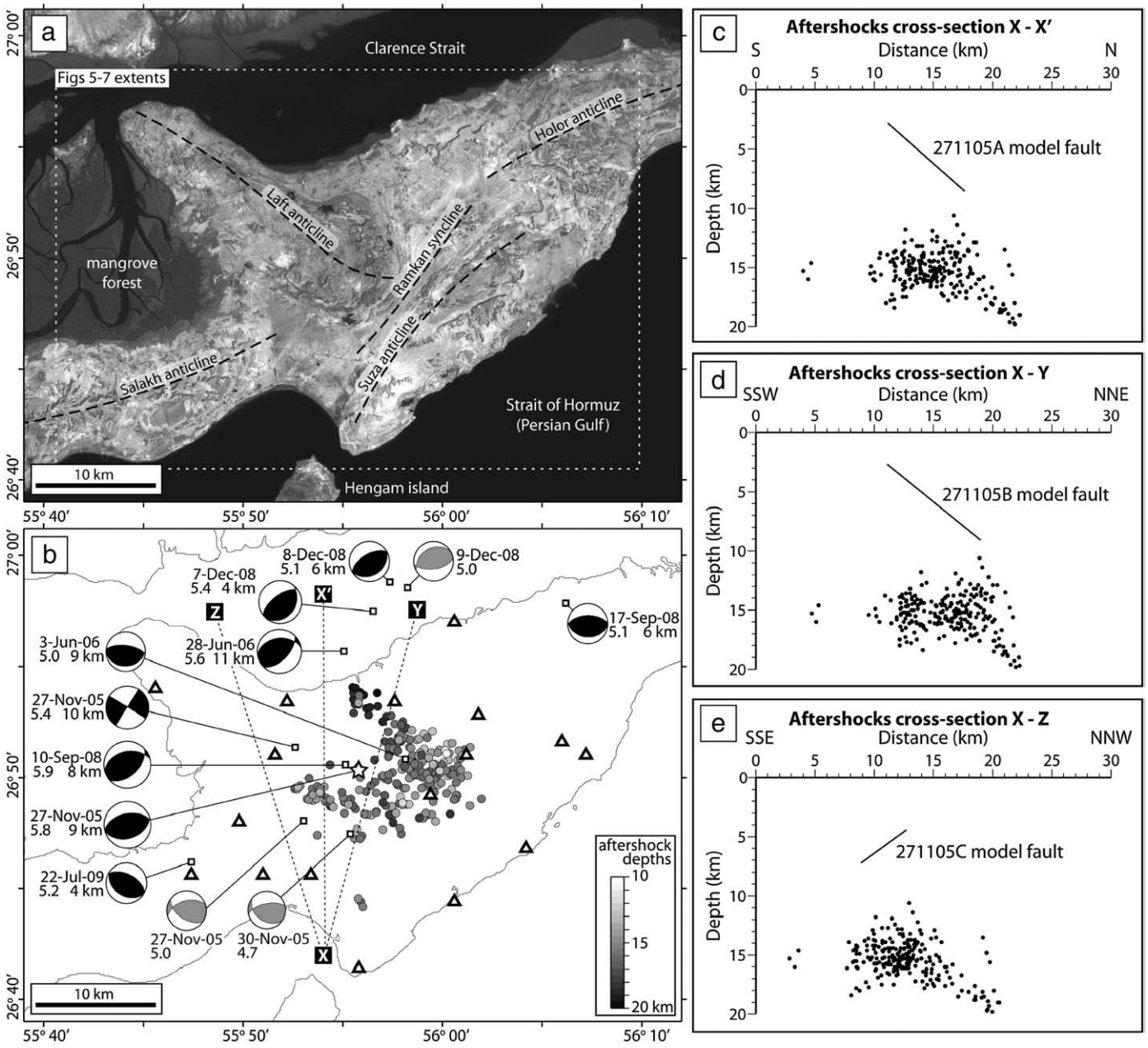

Fig. 4. (a) Landsat image (band 8) of central Qeshm island, with major fold axes marked as dashed lines (for a colour Landsat image, see Auxiliary Material, Fig. S6). (b) Earthquake focal mechanisms (November 2005–July 2009) and locally-recorded aftershock hypocenters (December 2005–February 2006) of the Qeshm island earthquake sequence. Black focal spheres are body-wave models of the largest nine events, with dates, moment magnitudes and centroid depths plotted next to them. Grey focal spheres are Global CMT mechanisms of three, smaller events, with dates and moment magnitudes. The star is the epicenter of the first earthquake, from InSAR modelling. Squares are epicenters of the other large earthquakes relative to this first event, from Hypocentroidal Decomposition. Small circles are hypocenters of the 244 best-located aftershocks, shaded according to depth. Temporary seismometers used to record these events are marked as triangles. (c) N–S section showing the projection of the 244 best-located aftershocks and model fault plane 271105A onto the line *X*–*X*′ (dashed line, (b)). This figure should not necessarily imply the absence of shallow aftershocks; these would have less well-constrained depths as a result of the station spacing. (d) NNE–SSW section showing the projection of aftershocks and model fault plane 271105B onto the line *X*–*Y*. (e) NNW–SSE section showing the projection of aftershocks and model fault plane 271105C onto the line *X*–Z.

the events in chronological order. In Section 4, we summarize our observations and discuss implications for deformation models of the Simply Folded Belt.

3.2. 27 November 2005 10:22 UTC earthquake (M_w 5.8)

The first earthquake in the Qeshm island sequence occurred at 10:22 UTC (13:52 local time) on 27 November 2005. The earthquake killed thirteen people and injured about 100, badly damaging a number villages in the central part of the island. Small cracks observed along the axis of the Ramkan syncline (Fig. 4) were attributed to minor bedding plane-slip, and there were otherwise no reports of surface rupturing (Nissen et al., 2007).

In a preliminary study, we estimated the source parameters of the earthquake from teleseismic body-waves and ground displacements measured with radar interferometry (Nissen et al., 2007). For the body-wave modelling we assumed a half-space of $V_p = 6.0$ km s^{-1}, $V_s = 3.45$ km s^{-1} and density 2800 kg m^{-3}, while for the elastic dislocation modelling, we used equivalent Lamé parameters, $\lambda = \mu = 3.2 \times 10^{10}$ Pa.

However, by inverting locally-recorded aftershock arrival times (Section 3.3.2) we find seismic velocities to be significantly lower than these values. In the remainder of this section, we reassess the

Table 1
Earthquake source parameters from seismology. Nine events were large enough to be modelled independently using teleseismically-recorded body-waves; source parameters for the three remaining earthquakes (marked with asterisks) are from the Global CMT catalogue. *Latitude* and *Longitude* are from hypocentroidal decomposition (see text), *FS* is the focal sphere, and *Z* is the centroid depth in km. We chose to use $V_p = 5.7$ m s^{-1}, $V_s = 3.3$ m s^{-1} and $\rho = 2.7 \times 10^3$ kg m^{-3}, based on the upper part of the velocity structure calculated in Section 3.3.2 by inverting locally-recorded aftershock arrival times.

Date	Time	Latitude	Longitude	Strike 1	Dip 1	Rake 1	Strike 2	Dip 2	Rake 2	FS	Z (km)	Moment (Nm)	Mw
27 Nov 2005	10:22	26.839°[a]	55.930°[a]	259	50	95	71	40	84		9	64.1×10^{16}	5.8
[b]27 Nov 2005	11:13	26.801°	55.884°	254	49	52	124	53	126		–	3.5×10^{16}	5.0
27 Nov 2005	16:30	26.856°	55.877°	212	89	358	302	88	181		10	15.8×10^{16}	5.4
[b]30 Nov 2005	15:19	26.791°	55.923°	258	62	62	127	39	132		–	1.2×10^{16}	4.7
3 Jun 2006	07:15	26.847°	55.969°	277	65	94	87	25	81		9	4.1×10^{16}	5.0
28 Jun 2006	21:02	26.928°	55.918°	264	41	124	42	57	64		11	27.2×10^{16}	5.6
10 Sep 2008	11:00	26.843°	55.919°	259	43	115	46	52	68		8	91.4×10^{16}	5.9
17 Sep 2008	17:43	26.964°	56.103°	269	56	88	93	34	93		6	5.2×10^{16}	5.1
7 Dec 2008	13:36	26.958°	55.942°	234	64	99	34	27	72		4	18.4×10^{16}	5.4
8 Dec 2008	14:41	26.980°	55.956°	240	59	91	58	31	88		6	4.8×10^{16}	5.1
[b]9 Dec 2008	15:09	26.976°	55.971°	241	33	73	81	59	101		–	4.3×10^{16}	5.0
22 Jul 2009	03:53	–	–	297	54	86	123	36	95		4	8.0×10^{16}	5.2

[a] Latitude and longitude fixed to agree with interferometry.
[b] Source parameters from the Global CMT catalogue.

earthquake source parameters using velocities that are consistent with those determined from aftershocks: $V_p = 5.7$ km s^{-1} (the average of the top two layers in the aftershock-derived velocity structure), $V_s = 3.3$ km s^{-1}, and density = 2700 kg m^{-3}. For the InSAR modelling we used a half-space with the equivalent elastic parameters $\lambda = \mu = 2.9 \times 10^{10}$ Pa, derived using the equation $V_p = ((\lambda + 2\mu)/\rho)^{0.5}$.

3.2.1. Teleseismic body-wave modelling

We followed the same body-wave modelling procedure as in the earlier paper, described in the Auxiliary material. Crucially, independent body-wave modelling of this sort can constrain the centroid depth of the earthquake better than the routinely low-pass filtered solutions reported by the Global CMT catalogue (e.g. Engdahl et al., 2006; Maggi et al., 2000; Talebian and Jackson, 2004). The centroid depth represents the average depth of the whole the earthquake slip distribution, and is different from the nucleation depth, which for these earthquakes is unconstrained by local data.

Our improved body-wave model has the same strike, dip, rake, and centroid depth as our preliminary solution, with reverse slip on a fault plane that dips either 50° N or 40° SSE (Table 1 and Fig. S1, Auxiliary material). However, the moment (0.64×10^{18} Nm) is ~10% lower than for the preliminary model, reducing the moment magnitude from 5.9 to 5.8. It is also lower than the Global CMT moment of 1.03×10^{18} Nm. The centroid depth remains unchanged at 9 km, and we estimated errors of ±3 km in this value (Auxiliary material). On its own, the body-wave model is therefore consistent with a source in the lower sedimentary cover or the uppermost basement.

3.2.2. Elastic dislocation modelling

For the elastic dislocation modelling, we used the same three interferograms as in our preliminary study, constructed from the Envisat Advanced Synthetic Aperture Radar (ASAR) data outlined in Table 2. Two of these are from descending (N to S) satellite orbits and have a WNW-facing look direction with a steep, 23° incidence angle (measured from the vertical). The third interferogram is from an ascending (S to N) orbit, with an ENE-facing look direction and a shallower, 41° incidence angle.

Two interferograms (one descending, one ascending) are shown in Fig. 5a–b; for space reasons, the third is shown in the Auxiliary Material (Fig. S7a). Each displays an elliptical pattern of fringes containing ground displacements toward from the satellite, and, to the SSW, a smaller area containing displacements away from the satellite. In Nissen et al. (2007), we showed that these displacements correspond mainly to uplift and subsidence, rather than to horizontal motions. There is no sharp division between the uplifted and subsided areas, consistent with buried rupture.

Using standard sampling and modelling procedures (e.g. Wright et al., 1999; details provided in Auxiliary material), we inverted the line-of-sight displacements for uniform slip on a rectangular fault plane in an elastic half-space. Because the two descending-track interferograms

Table 2
We used Advanced Synthetic Aperture Radar (ASAR) data from the European Space Agency (ESA) Envisat platform to construct all our interferograms (details of processing are provided in the Auxiliary material). Mode is the Envisat acquisition mode, and *i* is the incidence angle at the center of the image, measured from the vertical. The first image of each pair was acquired on Date 1, and the second on Date 2, separated by Δt days. The perpendicular baseline between the orbits in each pass is $B_\perp$ m, and the altitude of ambiguity H_a m.

Pass	Mode	*i*	Track	Date 1	Orbit 1	Date 2	Orbit 2	Δt (days)	$B_\perp$ (m)	H_a (m)	Earthquakes spanned
Desc.	IS2	23°	435	24-Nov-05	19,527	29-Dec-05	20,028	35	197	48	Nov-05 eqs
Desc.	IS2	23°	435	17-Feb-05	15,519	02-Feb-06	20,529	350	65	145	Nov-05 eqs
Asc.	IS6	41°	328	05-Jan-05	14,911	21-Dec-05	19,921	350	37	254	Nov-05 eqs
Desc.	IS2	23°	435	18-May-06	22,032	17-Apr-08	32,052	700	281	34	03-Jun-06, 28-Jun-06
Asc.	IS6	41°	328	10-May-06	21,925	25-Apr-07	26,935	350	116	81	03-Jun-06, 28-Jun-06
Asc.	IS6	41°	328	14-Jun-06	22,426	21-Mar-07	26,434	280	324	29	28-Jun-06
Desc.	IS2	23°	435	17-Apr-08	32,052	09-Oct-08	34,557	175	211	45	Sep-08 eqs
Desc.	IS2	23°	435	17-Apr-08	32,052	07-May-09	37,563	385	153	62	Sep-08 eqs, Dec-08 eqs
Asc.	IS6	41°	328	25-Apr-07	26,935	01-Oct-08	34,450	525	253	37	Sep-08 eqs
Asc.	IS6	41°	328	25-Apr-07	26,935	29-Apr-09	37,456	735	106	89	Sep-08 eqs, Dec-08 eqs
Desc.	IS2	23°	435	09-Oct-08	34,557	07-May-09	37,563	210	59	161	Dec-08 eqs
Asc.	IS6	41°	328	01-Oct-08	34,450	29-Apr-09	37,456	735	147	65	Dec-08 eqs
Desc.	IS2	23°	435	07-May-09	37,563	20-Aug-09	39,066	105	17	600	22-Jul-09
Asc.	IS6	41°	328	29-Apr-09	37,456	16-Sep-09	39,460	140	379	26	22-Jul-09

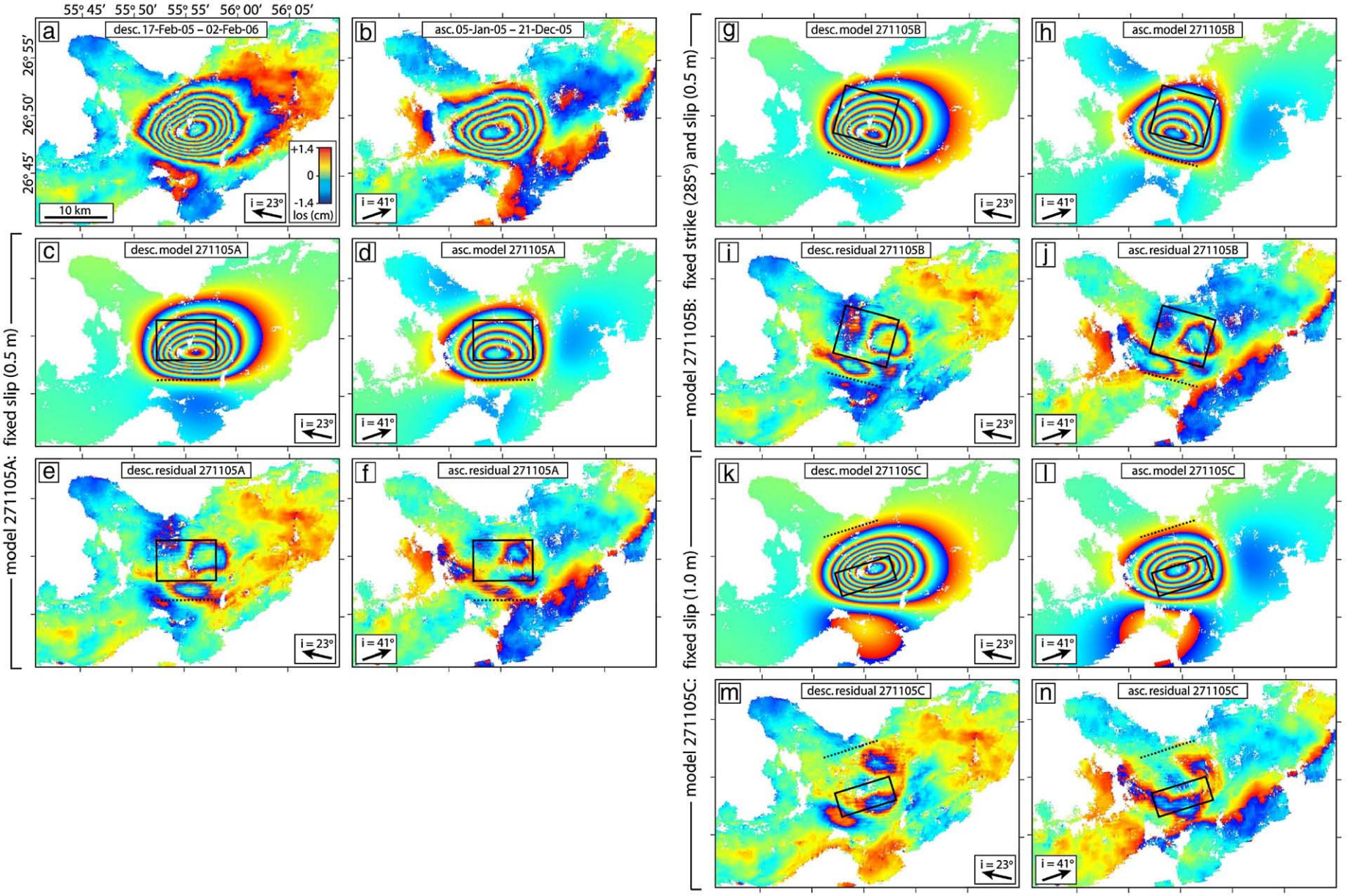

Fig. 5. Observed, model and residual interferograms for the 27 November 2005 earthquake. Panels on the left are descending-track interferograms and panels on the right are ascending-track interferograms; in each case, the satellite line-of-sight is represented by a black arrow and the incidence angle (measured from the vertical) by '*i*.' All interferograms are shown wrapped, each cycle of colour (or fringe) representing a displacement of one radar half-wavelength (2.8 cm) in the line-of-sight. Black rectangles outline the model fault planes in map view, and dotted black lines show their up-dip projection to the surface. (a) and (b) are observed interferograms. (c) and (d) are synthetic interferograms for model 271105A, and (e) and (f) are residual interferograms calculated by subtracting the model displacements from the actual data. (g)–(j) are synthetic and residual interferograms for model 271105B; (k)–(m) are synthetic and residual interferograms for model 271105C.

share the same look direction, they were each given half the weighting of the single, ascending-track interferogram in the inversion.

Our initial, best-fit solution yields several meters of slip on a fault with a width of less than 1 km. This high amount of slip and narrow fault-plane width are implausible given the magnitude of the earthquake (M_w ~6) and the length of the fault plane (~10 km). Empirical scaling relations show that earthquake slip-to-length ratios are typically in the order of 5×10^{-5} (Scholz, 1982). To attain a more realistic fault model, we therefore fixed the slip to a value of 0.5 m and solved for the remaining parameters. The resulting model — 271105A in Table 3 — involves almost pure reverse slip between depths of 2.8 km and 8.5 km, on a 9.6 km-long fault plane that dips 42° N. The strike, dip and rake agree to within ~10° of those of the N-dipping body-wave nodal plane (Table 1). However, the depth of the center of the fault plane (5.7 km) is somewhat shallower than the body-wave centroid depth (9±3 km), and the moment (1.20×10^{18} Nm) is almost double that of the body-wave model (0.64×10^{18} Nm). These discrepancies will be discussed in Section 4.

Model interferograms are shown in Fig. 5c–d, and residual interferograms (calculated by subtracting model displacements from observed ones, and displayed wrapped) are shown in Fig. 5e–f. The pattern of uplift is well-reproduced by the model, with residual displacements of up to one fringe (2.8 cm) in this area. However, the most closely-packed model fringes are on the S side of the uplifted area, rather than on the SSW side (as observed in the real interferograms). Model subsidence is also positioned a few kilometers east of its location in the data.

To address these problems, we inverted the data again using a fixed strike of 285°, thus forcing the model fault to trend parallel to the closely-packed fringes in the interferograms. The slip remained fixed at 0.5 m. The resulting model — 271105Bin Table 3 — involves a small right-lateral component (rake 114°), but the dip, length, depths and moment are all similar to those of model 271105A. Although the RMS misfit is slightly higher (0.55 cm) than for 271105A (0.49 cm), 271105B reproduces the closely-packed fringes better, and places subsidence in the correct area (Fig. 5g–j).

Next, we experimented with further inversions using different amounts of slip. We found a clear trade-off between slip and fault width: the higher the slip, the narrower the width of the fault plane. Fixing slip to 0.25 m significantly worsens the fit to the data relatively to the 0.5 m models. Doubling slip to 1.0 m, on the other hand, produces a slightly better match to the observed data, with an RMS misfit of 0.44 cm (model 271105C in Table 3 and Fig. 5k–n). This model comprises an SSE-dipping fault plane that projects to the surface along the north-western side of the uplifted area, rather than a N- or NNE-dipping fault plane that projects to the surface along the southern side of the uplifted area, as in models 271105A and 271105B. The fault length (9.1 km) and moment (1.25×10^{18} Nm) are similar to those of the ~N-dipping models, but the down-dip fault width is narrower, with slip occurring between depths of 4.4 km and 7.2 km. This reflects the trade-off between fault width and slip.

Our results are therefore consistent with slip on either a N- or NNE-dipping fault, or a SSE-dipping fault. Because 271105C best reproduces the position and magnitude of subsidence, and because its strike (73°) is consistent with that of the SSE-dipping body-wave nodal plane (71°), we marginally favour an SSE-dipping fault plane. However, given the small differences in RMS misfit (~0.1 cm), and the assumptions of uniform slip (and rake) on a planar, rectangular fault plane, we do not rule out a N- or NNE-dipping fault orientation.

More importantly for the purposes of this study, the earthquake depths are well constrained whichever of the models is correct, with depths of the center of each model fault plane at 5.7–5.8 km. Crucially, there is no trade-off between this central depth and fault slip, so rupture must have been concentrated within the lower part of the sedimentary cover. However, because of the trade-off between fault width and slip, we do not know whether the bottom of the fault plane also ruptured the uppermost crystalline basement.

To further test how tightly constrained these depths are, we also carried out distributed-slip inversions (e.g. Wright et al., 2003; details provided in Auxiliary material). The resulting models are non-unique, the precise slip patterns depending on the degree of smoothing imposed on the fault plane; furthermore, they only reduce the RMS misfits by a small amount (<0.1 cm) relative to the uniform slip models. Most importantly for the purposes of our study, the depth range over which significant slip occurs (>10 cm) is very similar to the extents of the uniform slip model fault planes. To illustrate this, we show an example of such a slip distribution (for the N-dipping model fault, 271105A) in the Auxiliary material (Fig. S8). The peak slip is at 5.7 km — the same as the central depth of the uniform slip model — and there are only small amounts of slip lying outside the bounds of the uniform slip model fault.

3.3. November 2005–February 2006 aftershocks

3.3.1. Teleseismic body-wave modelling

Two moderate magnitude aftershocks (M_w 5.0 and 5.4) occurred on 27 November 2005, followed by a third (M_w 4.7) on 30 November

Table 3
Earthquake source parameters for the 27 November 2005 (10:22 UTC), 28 June 2006 and 10 September 2008 earthquakes, from modelling line-of-sight surface displacements and with errors at the 1σ level. *FS* is the focal shere, and titLatitude and *Longitude* represent the surface projection of the center of the model fault plane. *L* is the length of the fault, and *Top*, *Bot* and *C* are the depths of the top, bottom and center of the fault plane, respectively (the last of these is equivalent to the centroid depth in Table 1). *RMS* is the root mean square misfit between model and data.

Model	Strike	Dip	Rake	FS	Slip (m)	Latitude	Longitude
271105A	270±3	42±3	104±5		0.50[a]	26.77°±0.3 km	55.92°±0.4 km
271105B	285[a]	39±3	114±3		0.50[a]	26.77°±0.3 km	55.90°±0.2 km
271105C	73±3	36±2	66±5		1.00[a]	26.88°±0.6 km	55.89°±0.5 km
280606	25±11	46±14	65±17		0.31±0.16	26.91°±1.9 km	55.89°±3.4 km
100908A	34±2	50±6	55±6		0.65±0.11	26.89°±0.3 km	55.89°±0.5 km
100908B–1	25[a]	48±6	50±5		0.50[a]	26.89°±0.5 km	55.90°±0.5 km
100908B–2	65[a]	49±11	62±21		0.50[a]	26.87°±1.8 km	55.86°±1.7 km

Model	*L* (km)	Top (km)	Bot (km)	*C* (km)	Moment (Nm)	M_w	RMS (cm)
271105A	9.6±0.3	2.8±0.1	8.5±0.5	5.7±0.2	$1.20\pm0.06\times10^{18}$	6.0	0.49
271105B	8.8±0.2	2.7±0.1	9.0±0.6	5.8±0.3	$1.30\pm0.07\times10^{18}$	6.0	0.55
271105C	9.1±0.3	4.4±0.2	7.2±0.3	5.8±0.2	$1.25\pm0.06\times10^{18}$	6.0	0.44
280606	17.0±3.7	5.0±1.4	12.0±2.1	8.5±1.2	$1.35\pm0.32\times10^{18}$	6.0	0.69
100908A	12.8±0.8	3.2±0.3	7.7±0.6	5.5±0.3	$1.41\pm0.17\times10^{18}$	6.0	1.12
100908B–1	10.1±1.0	2.4±0.2	8.8±1.1	5.6±0.6	$1.27\pm0.20\times10^{18}$	6.0	1.00
100908B–2	9.1±2.4	4.5±0.7	8.1±1.8	6.3±1.1	$0.59\pm0.15\times10^{18}$	5.8	1.00

[a] Fixed in inversion.

(Table 1). These events cannot be distinguished from the much larger mainshock in the interferograms, but focal mechanisms are available in the Global CMT catalogue, and the 27 November, 16:30 UTC earthquake is also large enough for independent body-wave modelling to constrain the centroid depth. Our solution for this event is shown in the Auxiliary Material (Fig. S1) and its source parameters are listed in Table 1. We obtained a strike–slip mechanism with a similar *P*-axis to that of the 10:22 mainshock, but it is not clear which nodal plane represents the fault. From the centroid depth of 10 ± 3 km, it is also uncertain whether the earthquake occurred in the uppermost basement or the lower sedimentary cover. Global CMT parameters for the smaller two events are also listed in Table 1; both involved oblique-slip, but precise depths are not available.

We used the Hypocentroidal Decomposition (HDC) method (Jordan and Sverdrup, 1981) to determine the positions of these (and subsequent) earthquakes relative to the 10:22 mainshock. The mainshock hypocenter was fixed at the center of the model 271105A fault plane (star, Fig. 4b). Positions of later, moderate magnitude earthquakes, relative to the mainshock, are shown as squares on Fig. 4b, linked to their focal mechanisms by black lines. Horizontal errors in these relative locations are typically 3–5 km. The 27 and 30 November earthquake hypocenters lie ~5 km from the mainshock, to the W (27 November, 16:30 UTC), SW (27 November, 11:13 UTC) and S (30 November, 15:19 UTC).

3.3.2. Locally-recorded aftershocks

We also determined the distribution of smaller aftershocks using data collected from a local network of nineteen portable, three-component seismometers. These were deployed in early December 2005 and recorded until late February 2006. Details of the instruments and data processing techniques can be found in Tatar et al. (2005).

During the seven week period recorded by our network, more than 1700 individual shocks were detected, ranging in magnitude from 1–4. At first, these were located using the Hypocenter 3.2 program (Lienert and Havskov, 1995), assuming a simple half-space of $V_p = 6.0$ km s^{-1}. We then selected a subset of 244 earthquakes with an azimuthal gap of $\leq 180°$, an RMS residual (the difference between observed and calculated arrival times) of ≤ 0.2 s, and at least 15 separate *S* and *P* phase recordings. We inverted the arrival times of this subset using the VELEST program (Kissling, 1988), which simultaneously calculates improved hypocenters and a best-fit, layered velocity structure, and used randomly perturbed starting models to ensure convergence to the final structure (e.g. Hatzfeld et al., 2003).

Our final velocity structure is shown in Table 4 and comprises three layers of $V_p = 5.5$ km s^{-1} (0–8 km), 5.9 km s^{-1} (8–12 km) and 6.2 km s^{-1} (below 12 km). It is not clear which layer boundary corresponds to the cover–basement interface, so the best we can say is that the model is consistent with a depth to basement of 10 ± 2 km. This value is close to the estimated stratigraphic thickness on the adjacent mainland (Fig. 2), and is also similar to the basement depth of ~11 km determined using the same methods at Ghir in the central SFB (Hatzfeld et al., 2003).

Improved hypocenters for the 244 best-located aftershocks are plotted on Fig. 4b and are listed in full in the Auxiliary Material (Table S1). The aftershocks are strongly clustered, most of them situated E of the InSAR-derived model faults, with smaller groups of aftershocks to the N and S. Aftershock depths range between 10 km and 20 km, with the majority of events at 14–17 km, presumably within the upper part of the basement. Because the depth at which aftershocks are best-located is related to the station spacing, there are likely to be some shallower events amongst the less well-resolved aftershocks. However, the best-located subset are significantly deeper than the mainshock rupture, and demonstrate that the upper crust is seismogenic to at least 20 km. These results indicate that the 27 November 2005 main shock did not rupture the full thickness of the seismogenic layer.

To explore the relationship between the mainshock rupture and aftershocks further, we constructed three cross-sections through these data, perpendicular to each of the three elastic dislocation models (Fig. 4c–e). In none of these sections do the aftershocks form a down-dip continuation to the model fault planes. However, some aftershocks do delineate an apparent, N-dipping structure, which may represent a fault in the basement.

Because aftershocks are concentrated within the lower layers of the minimum-misfit velocity structure, velocities in the upper 0–8 km layer are relatively poorly constrained. Reducing V_p here to 5.0 km s^{-1} — the same as that estimated from microseismicity at Ghir (Tatar et al., 2004) — raises the peak in aftershock depths from ~15 km to ~13 km, thus reducing the distance between aftershocks and mainshock rupture. However, even with this low value of V_p, the majority of the best-determined aftershock depths are still placed within the basement.

Table 4
Our preferred velocity structure, determined by inverting the arrival times of the 244 best-recorded aftershocks.

Layer	V_p	Depth of top
1	5.50 km/s	0 km
2	5.90 km/s	8 km
Half-space	6.20 km/s	12 km

3.4. 3 and 28 June 2006 earthquakes (M_w 5.0, 5.6)

3.4.1. Teleseismic body-wave modelling

Despite their moderate magnitudes, these two earthquakes caused considerable damage on Qeshm island, the 3 June 2006 earthquake killing two people and injuring four, and the larger 28 June 2006 earthquake injuring nine people. Body-wave models are shown in the Auxiliary Material (Fig. S2), source parameters are listed in Table 1, and focal mechanisms and relative hypocenters are plotted on Fig. 4b. The relocated 3 June epicenter lies ~4 km east of the 27 November 2005 epicenter, and is characterised by reverse slip on either a steep N-dipping fault plane, or a shallow S-dipping one. The larger 28 June epicenter occurred ~10 km north of the 27 November 2005 epicenter, and comprises oblique reverse slip on a fault plane that dips N (with a right-lateral component) or SE (with a left-lateral component). Centroid depths of 9 ± 3 km and 11 ± 3 km suggest that both earthquakes occurred close to the basement–cover interface. As for the 27 November 2005 earthquake, our body-wave moments for these earthquakes (4.1×10^{16} Nm for 6 June and 2.7×10^{17} Nm for 28 June) are lower than the Global CMT moments (6.5×10^{16} Nm and 6.4×10^{17} Nm, respectively).

3.4.2. Elastic dislocation modelling

Relatively few Envisat data were acquired over Qeshm island during 2006 and 2007, and the interferograms spanning the 28 June 2006 earthquake each encompass long time periods: nearly 2 years in the case of a single descending interferogram, and nearly 1 year in the case of two ascending interferograms (Table 2). Look directions and incidence angles are as for the earlier interferograms spanning the 27 November 2005 earthquake.

Two of the interferograms are shown in Fig. 6a–b; the third, ascending interferogram is shown in the Auxiliary Material (Fig. S7b). Each displays a NE–SW-oriented, elliptical pattern of fringes, containing displacements of up to two radar half-wavelengths (~6 cm) toward the satellite. Their spatial correspondence in ascending and descending data imply that they primarily reflect uplift, rather than horizontal motions. There are no clear areas of subsidence, above the level of atmospheric noise, in any of these interferograms.

Following the modelling procedure used in Section 3.2.2, we inverted the line-of-sight displacements to obtain best-fit source parameters. The two ascending-track interferograms were each weighted half relative to the single, descending one. From forward elastic dislocation models constructed using the best-fit body-wave

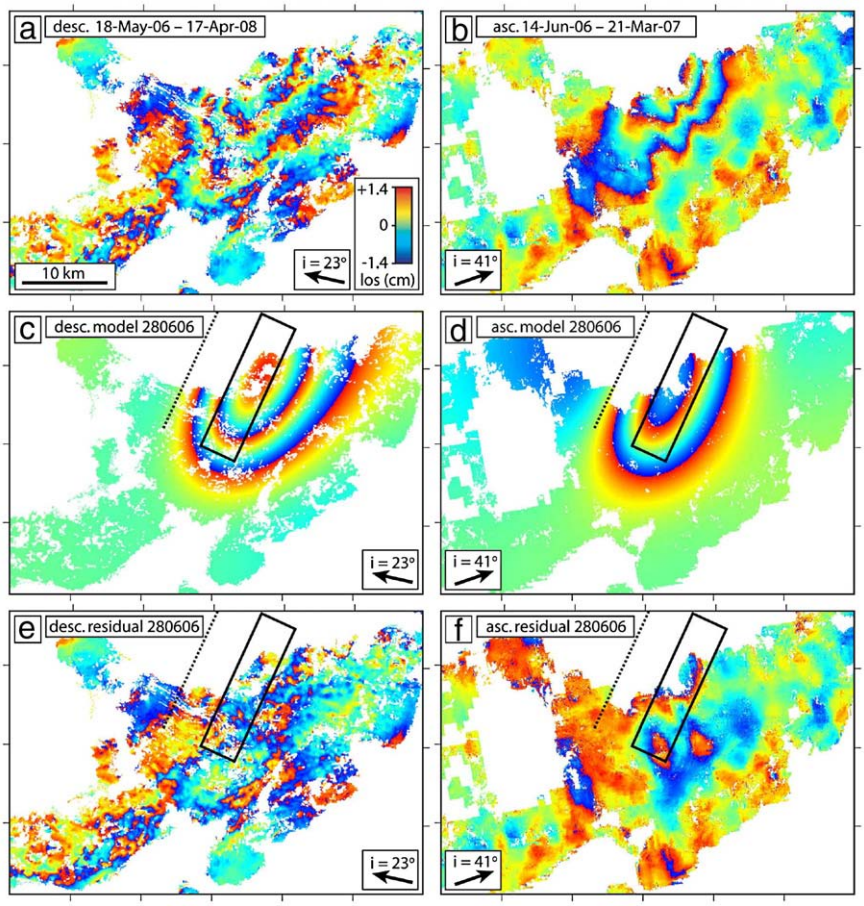

Fig. 6. Observed (a–b), model (c–d) and residual (e–f) interferograms for the 28 June 2006 earthquake. The layout and map extents are the same as in Fig. 5.

parameters, we expect the smaller 3 June earthquake to have contributed very little (less than one eighth of a fringe) to the overall InSAR signal, and we therefore solved for a single fault plane representing the larger 28 June event. The resulting model parameters are listed in Table 3, and model and residual interferograms are shown in Fig. 6c–f. Our model involves 0.31 m reverse slip, with a small left-lateral component, on a 17 km-long fault plane that dips 46° SE. Slip is buried to depths of 5.0–12.0 km, with the center point of the fault plane at 8.5 km, agreeing to within error with the body-wave centroid depth of 11 ± 3 km and close to the assumed position of the basement–cover interface. Given the uncertainty in the thickness of the cover, the earthquake may have ruptured the sedimentary cover, the basement, or a combination of the two.

Apart from a 17° discrepancy in strike, the position and orientation of the fault plane agree well the SE-dipping body-wave nodal plane of the 28 June earthquake (Table 1). The surface projection of the model fault trends perpendicular to the coastline of the Laft peninsula, close to (but north of) that of the 271105C fault plane. If the 271105C model is correct, the 28 June 2006 earthquake may have ruptured a north-eastern continuation of the same fault zone, although its hypocenter is positioned N of the 27 November 2005 earthquake, rather than to the NE (Fig. 4b). The geodetic moment (13.5×10^{17} Nm) is five times greater than the seismic moment from body-wave modelling (2.7×10^{17} Nm), and twice that of the Global CMT solution (6.4×10^{17} Nm). This discrepancy will be discussed in Section 4.

3.5. 10 September 2008 earthquake (M_w 5.9) and subsequent events

3.5.1. Teleseismic body-wave modelling

The 10 September 2008 earthquake was the largest earthquake in the Qeshm island sequence (M_w 5.9), and one of the most destructive, killing seven people and injuring at least 30. It was followed by aftershocks on 17 September (M_w 5.1), 7 December (M_w 5.4), 8 December (M_w 5.2), 9 December (M_w 5.0) and 22 July 2009 (M_w 5.2). Modelling body-waves, we determined source parameters for all but the smallest of these events (for which Global CMT parameters are available). Using HDC, we also determined relative epicenters for all but the 22 July 2009 earthquake. These results are listed in Table 1 and plotted on Fig. 4b.

The minimum-misfit focal mechanism for the largest earthquake, on 10 September 2008, is similar to that of the 28 June 2006 event, with reverse slip on a fault plane that dips N (with a right-lateral component) or SE (with a left-lateral component). The centroid depth is shallower, at 8 ± 3 km, and the HDC epicenter lies very close to the 27 November 2005 earthquake (Fig. 4b). The centroid depths of its largest aftershocks, determined from body-wave modelling, are also relatively shallow, ranging from ~4–6 km. The first of these (17 September) involved pure reverse slip on an E–W fault plane, and was located ~20 km NE of the two largest earthquakes, in eastern Qeshm island. The 7–9 December events form a cluster 15–20 km north of the mainshocks (in the Clarence Strait), and each involved reverse slip on NE–SW-trending fault planes. The 22 July 2009 earthquake involved reverse slip on a NW–SE trending fault plane. Its Global CMT epicenter lies in central Qeshm island, but we did not further constrain its position relative to the other earthquakes in the sequence.

3.5.2. Elastic dislocation modelling

Using the Envisat data in Table 2, we constructed two descending and two ascending interferograms spanning the 10 September 2008 and 17 September earthquakes. Two of these are shown in Fig. 7a–b; the other pair, which utilizes the same master images but which also incorporates the 7–9 December aftershocks, are shown in the Auxiliary Material (Fig. S7c–d). We also constructed two interferograms

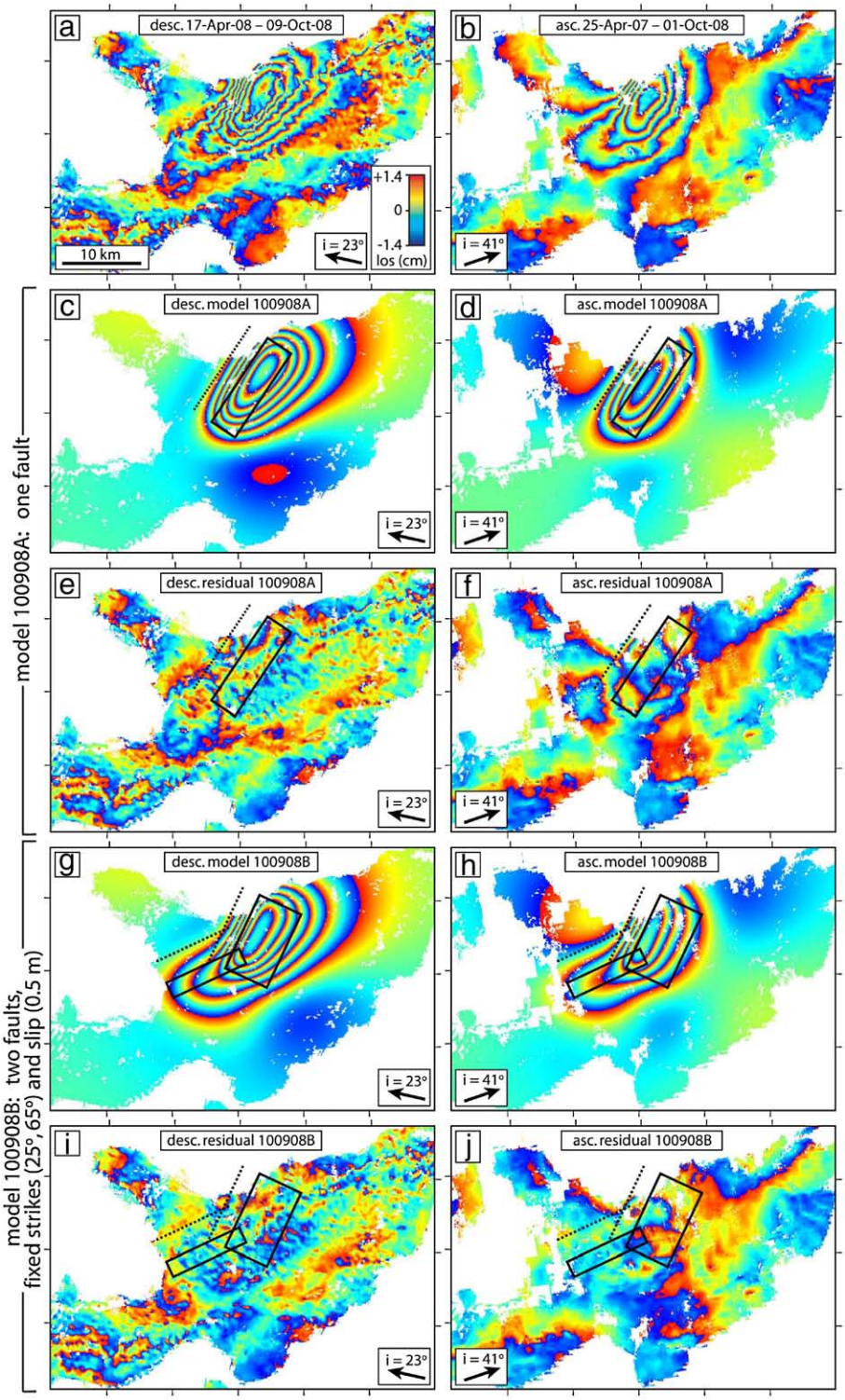

Fig. 7. Observed, model and residual interferograms for the 10 September 2008 earthquake. The layout and map extents are the same as in Fig. 5. (a) and (b) are observed interferograms. (c) and (d) are synthetic interferograms for model 091008A, and (e) and (f) are residual interferograms calculated by subtracting the model displacements from the actual data. (g)–(j) are synthetic and residual interferograms for model 091008B.

spanning only the 7–9 December earthquakes (Table 2), but these show no obvious coseismic signal (Fig. S7e–f), possibly because the 7–9 December epicenters lie in the Clarence Strait (Fig. 4b). A final pair of interferograms cover the 22 July 2009 event, but these also lack a clear earthquake signal (Fig. S7g–h).

Two of the 10 September 2008 interferograms are shown in Fig. 7a–b, while the other pair is shown in the Auxiliary Material (Fig. S7c–d). The descending-track data contain six fringes of line-of-sight displacements toward the satellite in northern Qeshm island, and a single fringe of displacements away from the satellite on the Laft peninsula. In the same places, ascending data contain four fringes of displacements toward the satellite, and two away from it. There is no sharp division between the displacements toward and away from the satellite, consistent with the buried slip. However, the most closely-packed fringes trend NE–SW across the northern Qeshm coastline, suggesting that this is where the rupture projects to the surface.

Next, we modelled the line-of-sight displacements to obtain the best-fitting earthquake source parameters. Only the shorter of the two ascending interferograms and the shorter of the two descending interferograms were used in the inversion, and these were given equal weighting. There is no clear, separate earthquake signal in the vicinity of the 17 September epicenter, so we solved for slip on a single fault plane, representing the larger, 10 September event.

Our initial source parameters are listed under model 1000908A in Table 3, and synthetic and residual interferograms are shown in Fig. 7c–f. The model comprises 0.65 m oblique (reverse and left-lateral) slip on a 12.8 km-long, SE-dipping fault plane. The top of the fault is at 3.2 km, the bottom at 7.7 km, and the central depth is 5.5 km, somewhat shallower than the centroid depth of 8 ± 3 km. This implies that the faulting ruptured the sedimentary cover, rather than the basement. The geodetic moment (1.41×10^{18} Nm) is higher than that of our body-wave model (0.91×10^{18} Nm), but slightly lower than that of the Global CMT solution (1.74×10^{18} Nm).

With an RMS misfit of 1.12 cm, this simple model reproduces the data well, but there are significant residuals close to the northern and southern ends of the model fault. However, we found that a simple, two-fault model provides a much improved fit in these areas. Faulting was represented as two discrete segments, with fixed strikes and slip (0.5 m) so as to reduce the number of variables. Experimenting with different combinations of strike and solving for the remaining parameters, we found that the best fit to the data (with an RMS misfit of 1.00 cm) was provided by segments with strikes of 25° and 65° (model 100908B in Table 3 and Fig. 7g–j). The two segments are ~10 km each in length, and line up end-to-end to form a kinked fault zone. The average strike of 45° is the same as that of the SE-dipping body-wave nodal plane. Rupture depths are similar to those of the single-fault model, with slip still restricted to the sedimentary cover. As for the 27 November 2005 earthquake, allowing distributed-slip on these model fault planes makes little difference to the depths at which significant slip occurs.

Interestingly, the orientations of the northern and southern segments are very similar to those of the SE-dipping 28 June 2006 model fault (Fig. 6c–d) and the SSE-dipping 27 November 2005 model fault (Fig. 5k–l), respectively. This raises the possibility that all three earthquakes ruptured a single, SE-dipping fault zone.

4. Discussion

4.1. Discrepancies in earthquake source parameters

All our InSAR-derived models have significantly higher moments than their respective body-wave models — by a factor of 2 for the 27 November 2005 earthquake, a factor of 5 for the 28 June 2006 earthquake and a factor of 1.5 for the 10 September 2008 earthquake. Many of the interferograms used to model these earthquakes also incorporate moderate magnitude aftershocks, but the combined seismic moments of these smaller events can account for only a small part of the moment deficits. Similar discrepancies were found for the Zagros earthquakes studied by Lohman and Simons (2005), with InSAR-derived moments up to six times higher than those of the Global CMT catalogue. The geodetic moment for the 25 March 2006 Fin earthquakes was also 50% higher than the combined moments from body-wave modelling (Roustaei et al., 2010).

Because the coseismic interferograms cover days, weeks or even months after the earthquakes, the higher InSAR-derived moments may reflect post-seismic deformation or small-magnitude aftershocks. We note, for instance, that the largest discrepancy in our study is for the 28 June 2006 earthquake, and that the coseismic interferograms used to model this event also span the longest post-seismic intervals. Whatever the underlying cause of the discrepancy, however, it appears to be a systematic one, affecting all earthquakes studied using these methods in the Simply Folded Belt.

We also found a discrepancy between the depths from elastic dislocation modelling and those from body-wave modelling. For each earthquake, the minimum-misfit centroid depth is similar to the depth of the bottom of the InSAR-derived fault plane, rather than the center of the fault plane, as might be expected. One possibility is that the extra moment detected using InSAR corresponds to shallow aseismic deformation (perhaps including after-slip) at the up-dip end of the fault plane. This would bring the top of the model fault plane closer to the surface, thus forcing the depth of its center to become shallower.

Although we used consistent seismic velocities and elastic parameters in the modelling, it is worth considering the effect that errors in these values would have on model depths. We found that reducing V_p to 5.0 km s^{-1} — the value estimated at Ghir (Tatar et al., 2004) — reduces seismic moments by ~20% and makes the centroid depth shallower by ~1 km. Reducing μ and λ by an equivalent amount, to 2.2×10^{10} Pa, also reduces the InSAR-derived moments by ~20%, but has no significant effect on the top and bottom fault-plane depths. An increase in V_p to 6.0 km s^{-1} increases seismic moments by ~10% and the centroid depths by ~0.5 km; evalues of μ and λ (3.2×10^{10} Pa) increase the geodetic moments by the same amount but again have little effect on the depth. Overall, these results suggest that realistic errors in the seismic parameters have little influence on differences between body-wave and InSAR depths, contributing at most ~1 km to the observed discrepancies.

4.2. Relations between buried faulting and surface folding

The 28 June 2006 and 10 September 2008 earthquakes occurred on SE-dipping fault planes that project to the surface along the northern Qeshm coastline. The dip-direction of the 27 November 2005 earthquake is uncertain, but it may have ruptured a western continuation of this same fault zone. These faults strike perpendicular to the SE-trending Laft anticline (Fig. 4a). If there were a connection between slip on the faults and the growth of the overlying folds, then the fold axes should be parallel, rather than perpendicular, to the strike of the faults. The Laft anticline must be decoupled from the faulting responsible for the Qeshm earthquakes, and is presumably a detachment fold.

Dislocation modelling of the interferograms suggests that the top of the faulting in the largest earthquakes (2–3 km) is at the expected levels of weak, marls in the middle part of the sedimentary cover (Fig. 2). By preventing earthquake slip from reaching shallower levels, these weak layers detach faulting in the underlying Competent Group from folding of the overlying strata. Similar arguments were used by Roustaei et al. (2010) for the 25 March 2006 earthquakes at Fin, where the detachment horizon was assumed to lie in the Gurpi marls. Mishan marls are exposed at the surface in the core of the Laft anticline, and a top rupture depth of 2–3 km thus corresponds to the Gurpi marls here, too.

Many authors have noted that some anticlines in the SFB are strongly asymmetric, with steeply dipping or even overturned southern limbs (e.g. Colman-Sadd, 1978; Falcon, 1969; McQuarrie, 2004; Molinaro et al., 2005). These shapes are consistent with growth above reverse faults that approach the surface, suggesting that the weak layers decoupling faulting and folding at Fin and Qeshm do so locally, rather than forming a regional d'ecollement. The Simply Folded Belt probably encompasses a combination of detachment folding above weak layers in the sedimentary cover, and forced folds above buried reverse faults.

4.3. Relations between mainshock depths and locally-recorded microseismicity

From the high-quality locally-recorded aftershock data, the upper crust at Qeshm island appears to be seismogenic to a depth of ~20 km.

This is similar to the maximum depth of locally-recorded microseismicity at Ghir in the central SFB (Tatar et al., 2004), though slightly shallower than the maximum depths of ~25 km recorded at Fin for aftershocks of the 25 March 2006 earthquakes (Roustaei et al., 2010). It is also consistent with the deepest waveform-determined centroid depths for M_w 5–6 earthquakes in the SFB, which are 17–18 km (Talebian and Jackson, 2004).

Our InSAR-derived models for the two largest earthquakes in the Qeshm island sequence are consistent with rupture of the lower part of the sedimentary cover, with bottom fault depths of 7–9 km. The depth to basement inferred from locally-recorded aftershock arrival times is 10 ± 2 km (Section 3.3.2). Together, these depths are consistent with ruptures that were terminated, or at least strongly attenuated, by the mechanically-weak Hormuz Salt formation at the base of the sedimentary cover. Rupture in the first earthquake must nevertheless have caused stresses in the underlying basement, that triggered the cloud of aftershocks at depths of 10–20 km. There are a number of possible triggering mechanisms, including loading, Coulomb stress changes, and dynamic stress transfer, but these are beyond the scope of this study and will be investigated in another paper. A similar pattern was also observed following the 25 March 2006 Fin earthquakes (Roustaei et al., 2010), although station coverage in the Fin area was relatively poor and the aftershock depths are consequently less well constrained than for those detected at Qeshm. However, vertical separations of shallow, mainshock ruptures and deeper aftershocks have also been observed outside the Simply Folded Belt — at Bam, in eastern Iran (Jackson et al., 2006; Tatar et al., 2005), and at Tottori, in Japan (Semmane et al., 2005). In these cases there are no known, mechanically-weak layers at depth with which to explain the separation.

By considering regional earthquake magnitudes, we can investigate whether the Hormuz salt provides a significant barrier to rupture propagation across the whole SFB, or whether this behaviour might be restricted to Qeshm and Fin. If the whole 20 km thickness of the seismogenic layer ruptured in a single earthquake, and assuming a dip of 45°, a rupture length equal to its width (28 km), and a slip-to-length ratio of 5×10^{-5}, one would expect an earthquake of $M_w \sim 7.0$. But if only half the seismogenic layer was ever to rupture in a single event, and applying the same scaling arguments, earthquake magnitudes should be limited to much lower values, of $M_w \sim 6.3$.

The largest instrumentally-recorded events in the Simply Folded Belt are the M_w 6.7 earthquakes at Ghir (10 April 1972) and Khurgu (21 March 1977). Both these earthquakes are associated with strongly asymmetric anticlines, which expose otherwise rare Paleozoic strata at the surface and across which significant changes in the stratigraphic level and elevation are observed (Berberian, 1995). From our earthquake scaling arguments, we interpret these as rare earthquakes that may have ruptured through the basement–cover interface. However, apart from one other event — the M_w 6.5 Furg earthquake (10 November 1990), which ruptured the High Zagros Fault at the northern edge of the SFB (Walker et al., 2005) — all other earthquakes in the SFB in the last fifty years have moment magnitudes of ≤ 6.2. This suggests that across the region, the Hormuz salt (and potentially other weak horizons) forms an important barrier to rupture, and provides an important upper bound on the magnitudes of most reverse faulting earthquakes.

5. Conclusions

We investigated a cluster of three large earthquakes (27 November 2005, 28 June 2006 and 10 September 2008) and numerous smaller shocks at Qeshm island in the Zagros Simply Folded Belt. Surface displacements of first earthquake are best explained by buried slip on a SSE-dipping fault, although N- or NE-dipping faults can also account for the observed data. Whatever the fault orientation, the top and bottom depths of the rupture surface are consistent with faulting embedded within the competent, lower part of the sedimentary cover. However, locally-recorded aftershocks are reliably and resolvably located at depths of 10–20 km, and were thus concentrated within the underlying basement. We suggest that the vertical separation of mainshock and aftershock reflects the regional influence of the Hormuz salt, which forms a barrier to rupture at the base of the cover. The position of the 28 June 2006 earthquake in relation to this interface is less clear, but the 10 September 2008 earthquake also ruptured the lower sedimentary cover. These later earthquakes both ruptured SE-dipping faults, possibly a north-eastern continuation of the 27 November 2005 fault. The NE strike of this buried fault zone is perpendicular to the SE trend of the overlying Laft anticline, indicating that locally, faulting and folding must be decoupled. The top depth of the ruptures, at 2–3 km, suggests that this detachment occurs amongst mechanically-weak marls in the middle part of the sedimentary cover.

Acknowledgments

This work was supported by the Natural Environmental Research Council (NERC) funding of COMET, which is part of the National Center for Earth Observation (NCEO). All ENVISAT ASAR data are copyrighted by the European Space Agency and were provided under project AOE-621. We thank E.R. Engdahl for giving us access to his updated EHB catalogue, and we are grateful to Rowena Lohman and an anonymous reviewer for their constructive comments.

Appendix A. Supplementary data

Supplementary data associated with this article can be found, in the online version, at doi:10.1016/j.epsl.2010.04.049.

References

Adams, A., Brazier, R., Nyblade, A., Rodgers, A., Al-Amri, A., 2009. Source parameters for moderate earthquakes in the Zagros Mountains with implications for the depth extent of seismicity Jun. Bull. Seismol. Soc. Am. 99, 2044–2049.

Agard, P., Omrani, J., Jolivet, L., Mouthereau, F., 2005. Convergence history across Zagros (Iran): constraints from collisional and earlier deformation Jul. Int. J. Earth Sci. 94, 401–419.

Alavi, M., 2007. Structures of the Zagros fold–thrust belt in Iran Nov. Am. J. Sci. 307, 1064–1095.

Allen, M.B., Armstrong, H.A., 2008. Arabia Eurasia collision and the forcing of mid-Cenozoic global cooling. Palaeogeogr. Palaeoclimatol. Palaeoecol. 265, 52–58.

Authemayou, C., Bellier, O., Chardon, D., Benedetti, L., Malekzade, Z., Claude, C., Angeletti, B., Shabanian, E., Abbassi, M.R., 2009. Quaternary slip-rates of the Kazerun and the Main Recent Faults: active strike–slip partitioning in the Zagros fold-and-thrust belt Jul. Geophys. J. Int. 178, 524–540.

Baker, C., Jackson, J., Priestley, K., 1993. Earthquakes on the Kazerun Line in the Zagros Mountains of Iran: strike–slip faulting within a fold-and-thrust belt Oct. Geophys. J. Int. 115, 41–61.

Berberian, M., 1995. Master blind thrust faults hidden under the Zagros folds: active basement tectonics and surface morphotectonics Jan. Tectonophysics 241, 193–224.

Berberian, M., Papastamatiou, D., 1978. Khurgu (north Bandar Abbas, Iran) earthquake of March 21, 1977: a preliminary field report and a seismotectonic discussion Apr. Bull. Seismol. Soc. Am. 68, 411–428.

Blanc, E.J.-P., Allen, M.B., Inger, S., Hassani, H., 2003. Structural styles in the Zagros Simple Folded Zone, Iran May J. Geol. Soc. London 160, 401–412.

Colman-Sadd, S.P., 1978. Fold development in Zagros simply folded belt, Southwest Iran. Am. Assoc. Pet. Geol. Bull. 62, 984–1003.

Engdahl, E.R., van der Hilst, R.D., Buland, R., 1998. Global teleseismic earthquake relocation from improved travel times and procedures for depth determination Jun. Bull. Seismol. Soc. Am. 88, 722–743.

Engdahl, R.E., Jackson, J.A., Myers, S.C., Bergman, E.A., Priestley, K., 2006. Relocation and assessment of seismicity in the Iran region Nov. Geophys. J. Int. 167, 761–778.

Falcon, N.L., 1969. Problems of the relationship between surface structure and deep displacements illustrated by the Zagros Range. Time and Place in Orogeny. Special Publications No. 3. Geological Society of London, pp. 9–21.

Haghipour, A., Fontugne, M., 1993. Quaternary uplift of Qeshm Island (Iran). Comptes Rendus de l'Académie des Sciences 317, 419–424.

Hatzfeld, D., Tatar, M., Priestley, K., Ghafory-Ashtiany, M., 2003. Seismological constraints on the crustal structure beneath the Zagros Mountain belt (Iran) Nov. Geophys. J. Int. 155, 403–410.

Hessami, K., Koyi, H.A., Talbot, C.J., 2001a. The significance of strike–slip faulting in the basement of the Zagros fold and thrust belt. J. Pet. Geol 24, 5–28.

Hessami, K., Koyi, H.A., Talbot, C.J., Tabasi, H., Shabanian, E., 2001b. Progressive unconformities within an evolving foreland fold thrust belt, Zagros Mountains. J. Geol. Soc. London 158, 969–981.
Jackson, J., Bouchon, M., Fielding, E., Funning, G., Ghorashi, M., Hatzfeld, D., Nazari, H., Parsons, B., Priestley, K., Talebian, M., Tatar, M., Walker, R., Wright, T., 2006. Seismotectonic, rupture process, and earthquake-hazard aspects of the 2003 December 26 Bam, Iran, earthquake Sep. Geophys. J. Int. 166, 1270–1292.
Jackson, J., McKenzie, D., 1988. The relationship between plate motions and seismic moment tensors, and the rates of active deformation in the Mediterranean and Middle East Apr. Geophys. J. Int. 93, 45–73.
Jackson, J.A., 1980. Reactivation of basement faults and crustal shortening in orogenic belts Jan. Nature 283, 343–346.
Jahani, S., Callot, J.-P., Letouzey, J., Frizon de Lamotte, D., 2009. The eastern termination of the Zagros fold-and-thrust belt, Iran: Structures, evolution, and relationships between salt plugs, folding, and faulting. Tectonics 28, TC6004.
Jordan, T.H., Sverdrup, K.A., 1981. Teleseismic location techniques and their application to earthquake clusters in the South-Central Pacific. Bull. Seismol. Soc. Am. 71, 1105–1130.
Kent, P.E., 1979. The emergent Hormuz salt plugs of southern Iran. J. Pet. Geol 2, 117–144.
Kissling, E., 1988. Geotomography with local earthquake data Nov. Rev. Geophys. 26, 659–698.
Kugler, A., 1973. An interpretation of the Southwest Iran aeromagnetic survey, unpublished 1205. Oil Service Company of Iran.
Lienert, B.R., Havskov, J., 1995. Hypocenter 3.2: a computer program for locating earthquakes locally, regionally and globally. Seisnol. Res. Lett. 26–36.
Lohman, R.B., Simons, M., 2005. Locations of selected small earthquakes in the Zagros mountains Mar. Geochem. Geophys. Geosyst. 6, Q03001.
Maggi, A., Jackson, J.A., Priestley, K., Baker, C., 2000. A re-assessment of focal depth distributions in southern Iran, the Tien Shan and northern India: do earthquakes really occur in the continental mantle? Dec. Geophys. J. Int. 143, 629–661.
Masson, F., Chéry, J., Hatzfeld, D., Martinod, J., Vernant, P., Tavakoli, F., Ghafory-Ashtian i, M., 2005. Seismic versus aseismic deformation in Iran inferred from earthquakes and geodetic data Jan. Geophys. J. Int. 160, 217–226.
McQuarrie, N., 2004. Crustal scale geometry of the Zagros fold-thrust belt, Iran Mar. J. Struct. Geol. 26, 519–535.
McQuarrie, N., Stock, J.M., Verdel, C., Wernicke, B.P., 2003. Cenozoic evolution of Neotethys and implications for the causes of plate motions Oct. Geophys. Res. Lett. 30 (20), 2036.
Molinaro, M., Leturmy, P., Guezou, J.-C., Frizon de Lamotte, D., Eshraghi, S.A., 2005. The structure and kinematics of the southeastern Zagros fold-thrust belt, Iran: from thin-skinned to thick-skinned tectonics Jun. Tectonics 24, TC3007.
Morris, P., 1977. Basement structure as suggested by aeromagnetic surveys in SW Iran. Internal report, Oil Serivce Company of Iran.
Mouthereau, F., Tensi, J., Bellahsen, N., Lacombe, O., De Boisgrollier, T., Kargar, S., 2007. Tertiary sequence of deformation in a thin-skinned/thick-skinned collision belt: the Zagros Folded Belt (Fars, Iran) Sep. Tectonics 26, TC5006.
Nissen, E., Ghorashi, M., Jackson, J., Parsons, P., Talebian, M., 2007. The 2005 Qeshm Island earthquake (Iran) — a link between buried reverse faulting and surface folding in the Zagros Simply Folded Belt? Oct. Geophys. J. Int. 171, 326–338.
O'Brien, C.A.E., 1957. Salt diapirism in south Persia. Geol. Mijnbouw 19, 357–376.
Oveisi, B., Lavé, J., van der Beek, P., Carcaillet, J., Benedetti, L., Aubourg, C., 2009. Thick- and thin-skinned deformation rates in the central Zagros simple folded zone (Iran) indicated by displacement of geomorphic surfaces Feb. Geophys. J. Int. 176, 627–654.
Peyret, M., Rolandone, F., Dominguez, S., Djamour, Y., Meyer, B., 2008. Source model for the Mw 6.1, 31 March 2006, Chalan-Chulan Earthquake (Iran) from InSAR. Terra Nova 20, 126–133.
Pirazzoli, P., Reyss, J.L., Fontugne, M., Haghipour, A., Hilgers, A., Kasper, H.U., Nazari, H., Preusser, F., Radtke, U., 2004. Quaternary coral-reef terraces from Kish and Qeshm Islands, Persian Gulf: new radiometric ages and tectonic implications. Quat. Int. 120, 15–27.
Reyss, J.L., Pirazzoli, P.A., Haghipour, A., Hatt'e, C., Fontugne, M., 1998. Quaternary marine terraces and tectonic uplift rates on the south coast of Iran. Geol. Soc. London Spec. Publ. 146, 225–237.
Roustaei, M., Nissen, E., Abbassi, M., Gholamzadeh, A., Ghorashi, M., Tatar, M., Yamini-Fard, F., Bergman, E., Jackson, J., Parsons, B., 2010. The 25 March 2006 Fin earthquakes (Iran) — insights into the vertical extents of faulting in the Zagros Simply Folded Belt. Geophys. J. Int. 181, 1275–1291.
Scholz, C.H., 1982. Scaling laws for large earthquakes: consequences for physical models. Bull. Seismol. Soc. Am. 72, 1–14.
Semmane, F., Cotton, F., Campillo, M., 2005. The 2000 Tottori earthquake: a shallow earthquake with no surface rupture and slip properties controlled by depth Mar. J. Geophys. Res. 110 (B9), 03306.
Sherkati, S., Letouzey, J., Frizon de Lamotte, D., 2006. Central Zagros fold-thrust belt (Iran): new insights from seismic data, field observation, and sandbox modeling Jul. Tectonics 25, TC4007.
Sherkati, S., Molinaro, M., Frizon de Lamotte, D., Letouzey, J., 2005. Detachment folding in the Central and Eastern Zagros fold-belt (Iran): salt mobility, multiple detachments and late basement control Sep. J. Struct. Geol. 27, 1680–1696.
Stöcklin, J., 1968. Structural history and tectonics of Iran: a review Jul. Am. Assoc. Pet. Geol. Bull. 52, 1229–1258.
Talebian, M., 2003. Active faulting in the Zagros mountains of Iran. Ph.D. thesis, University of Cambridge.
Talebian, M., Jackson, J., 2002. Offset on the Main Recent Fault of NW Iran and implications for the late Cenozoic tectonics of the Arabia–Eurasia collision zone. Geophys. J. Int. 150, 422–439.
Talebian, M., Jackson, J., 2004. A reappraisal of earthquake focal mechanisms and active shortening in the Zagros mountains of Iran Mar. Geophys. J. Int. 156, 506–526.
Tatar, M., Hatzfeld, D., Ghafory-Ashtiany, M., 2004. Tectonics of the Central Zagros (Iran) deduced from microearthquake seismicity Feb. Geophys. J. Int. 156, 255–266.
Tatar, M., Hatzfeld, D., Moradi, A.S., Paul, A., 2005. The 2003 December 26 Bam earthquake (Iran), Mw 6.6, aftershock sequence Oct. Geophys. J. Int. 163, 90–105.
Vernant, P., Nilforoushan, F., Hatzfeld, D., Abbassi, M.R., Vigny, C., Masson, F., Nankali, H., Martinod, J., Ashtiani, A., Bayer, R., Tavakoli, F., Chéry, J., 2004. Present-day crustal deformation and plate kinematics in the Middle East constrained by GPS measurements in Iran and northern Oman Apr. Geophys. J. Int. 157, 381–398.
Walker, R.T., Andalibi, M.J., Gheitanchi, M.R., Jackson, J.A., Karegar, S., Priestley, K., 2005. Seismological and field observations from the 1990 November 6 Furg (Hormozgan) earthquake: a rare case of surface rupture in the Zagros mountains of Iran Nov. Geophys. J. Int. 163, 567–579.
Walpersdorf, A., Hatzfeld, D., Nankali, H., Tavakoli, F., Nilforoushan, F., Tatar, M., Vernant, P., Chéry, J., Masson, F., 2006. Difference in the GPS deformation pattern of North and Central Zagros (Iran) Dec. Geophys. J. Int. 167, 1077–1088.
Wright, T.J., Lu, Z., Wicks, C., 2003. Source model for the M_w 6.7, 23 October 2002, Nenana Mountain Earthquake (Alaska) from InSAR Sep. Geophys. Res. Lett. 30 (18), 1974.
Wright, T.J., Parsons, B.E., Jackson, J.A., Haynes, M., Fielding, E.J., England, P.C., Clarke, P.J., 1999. Source parameters of the 1 October 1995 Dinar (Turkey) earthquake from SAR interferometry and seismic bodywave modelling Oct. Earth Planet. Sci. Lett. 172, 23–37.